PAPER • OPEN ACCESS

Precipitation, strength and work hardening of age hardened aluminium alloys

To cite this article: Ø Ryen et al 2015 IOP Conf. Ser.: Mater. Sci. Eng. **89** 012013

View the article online for updates and enhancements.

Precipitation, strength and work hardening of age hardened aluminium alloys

Ø Ryen[1], B Holmedal[2], K Marthinsen[2] and T Furu[3]

[1]Oceaneering Asset Integrity, Havnegata 7, 7010 Trondheim, Norway
[2]Norwegian Department of Material Science and Engineering, University of Science and Technology, Alfred Getz veg 2, 7491 Trondheim, Norway
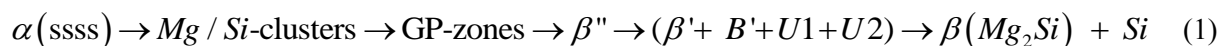[3]Norsk Hydro ASA, Corporate Technology office, 6600 Sunndalsøra, Norway

E-mail: bjorn.holmedal@ntnu.no

Abstract. The strength and work hardening of age hardened AA6063 and AA6082 alloys have been investigated in terms of a detailed characterization of precipitate and dislocation structures obtained by TEM and SEM. Tensile and compression tests were performed at as quenched, peak aged and severely aged conditions. A strong work hardening in the as quenched condition was found, similar to AlMg alloys with twice as much alloying elements in solid solution. It was found that the initial work hardening rate and the critical failure strain are both smallest at the peak aged condition. During large deformations the needle-shaped precipitates are sheared uniformly by dislocations altering their <001> orientations, which indicates extensive cross slip. In the overaged condition the early initial work hardening is larger than at the peak aged condition, but followed by a weak linear work hardening, apparently directly entering stage IV at a low strain. Cracked, needle-shaped precipitates were seen at larger strains.

1. Introduction

Precipitation of thermodynamically metastable or stable phases in age-hardenable aluminium alloys enables design of a variety of strong and light alloys. Due to a good ductility many of these alloys are applicable for energy absorption applications in safety constructions for military or transportation purposes. In terms of high volume production the AA6xxx alloys are very important with less expensive alloying elements. With recent improvements of analysing techniques, such as high-resolution TEM and atom probe microscopy, it has become possible to identify nearly all the phases present, and to visualise very small details as atomic clusters. The precipitation sequence may be written as:

$$\alpha\left(\text{ssss}\right) \rightarrow Mg\,/\,Si\text{-clusters} \rightarrow \text{GP-zones} \rightarrow \beta'' \rightarrow (\beta' + B' + U1 + U2) \rightarrow \beta\left(Mg_2Si\right) + Si \quad (1)$$

From the solid solution, several types of atomic clusters with various amounts of Mg and Si are formed [1, 2]. The clusters gradually transform into GP-zones, which are more related to the crystallography of the matrix [3], and further into β''-precipitates. β'' has been established as a monoclinic Mg_5Si_6-phase [4], and its occurrence is often observed to coincide with the maximum strength of the alloy (T6). Upon overageing several types of particles are formed, such as B', β' and β,

the latter one being the equilibrium phase Mg_2Si. Si-particles may also be formed. Other phases have been found as well, and even more will probably come. In Al-Mg-Si-Cu alloys, for example, variants of a Q-phase are identified [5, 6].

At room temperature the sequence will normally be limited to clustering, while commercial annealing temperatures (150-190°C) will give GP-zones and β'', as well as several phases if the annealing time is long enough. Even higher temperatures are required to form the equilibrium phase.

Deformation structures are directly linked to the interaction between dislocations and obstacles in the material. Several authors have treated this topic in detail, e.g. Ashby [7] and Brown and Ham [8] and Ardell [9]. Humphreys and Hatherly [10] give a thorough description of the evolution of deformation structures in various alloys. The large number of publications from the Risø-group [11-13] provide rich evidence for the development of substructure in pure aluminium and Al-Mg alloys. Pure aluminium and low solute alloys generally exhibit a cell- or subgrain structure, i.e. the dislocations organise themselves into boundaries surrounding volumes of a low dislocation density. This self-organisation is limited by the presence of solute atoms, giving a lower rate of dynamic recovery and less well-defined subgrain structure. When the Mg content reaches 4-5% the alloy is often termed non-cell forming. A work by Korbel et al. [14] describes such a microstructure and strain localisation in Al-Mg.

A few articles exist where the deformation structure of aged Al-Mg-Si alloys are studied. It is generally observed that underaged samples get a uniform distribution of dislocations, while the dislocations localise into bands in peak aged samples [15, 16]. This banding is often assumed to be related to the shearing of precipitates, creating softer traces for the dislocation slip. The phenomenon is reported for other age-hardenable alloys as well, i.e. Al-Cu, Al-Li and Al-Zn-Mg [17-19]. Also Dowling and Martin [20] observed these dislocation bands in Al-Mg-Si, and found that if strong particles (dispersoids) were present along with the precipitates the bands disappeared after a few percent strain.

In addition to the development of a dislocation structure, it is of great interest to understand the performance of the precipitates during deformation. As mentioned, the precipitates present at peak hardness are shearable, which is evidenced by the in-situ TEM work of Vivas et al. [21] on an AA6056 alloy. After heavy deformation of peak aged alloys the shearable precipitates dissolve, i.e. they are cut into so small pieces that they become thermodynamically unstable [22-24].

In overaged conditions the precipitates are to a larger extent non-shearable, i.e. they remain undeformed while the matrix around them is deformed. Poole et al. [25] have observed that this is the case for small strain deformation of an Al-Mg-Si-Cu alloy, and that dislocations tangle around the precipitates. When the strain exceeds 20% (in cold rolling) the long rod/lath-shaped precpitates are seen to be fragmented into shorter segments. Nourbakhsh and Nutting [23] observed the same after cold rolling of an overaged Al-Cu alloy. They related the low, and partially negative, work hardening rate of the overaged condition to such a fragmentation of the θ'-plates.

An important and promising application of AA6xxx alloys is in the crash-components of vehicles. Therefore, the properties defining the crashworthiness of such alloys are of great interest. The yield strength is important in order to resist deformation, while the ability to work harden has a significant impact on the energy absorption capacity. In order to avoid cracking and failure the ductility (uniform strain, fracture strain) should not be too low. A parameter that has gained attention is the critical failure strain (CFS), [26] defined from a tensile test by:

$$CFS = -\ln\left(1 - \left(\tfrac{1}{2}e_u + \left(1 - \tfrac{1}{2}e_u\right)\left(1 - R_f/R_m\right)\right)\right) \tag{2}$$

where e_u is the nominal uniform elongation and R_f and R_m are the nominal fracture stress and maximum stress, respectively. This parameter basically reflects the reduction in area in the neck of a tensile test specimen.

The variation in yield strength of Al-Mg-Si alloys, and other age-hardenable alloys, as a function of ageing time and temperature has been studied extensively, and several groups have provided good

models for this important mechanical property [27-29]. Much less attention has been paid to the influence of a precipitate structure on the work hardening behaviour, especially when it comes to large strains. Cheng et al. [30-33] studied the work hardening of several tempers of AAxxx and AA7xxx alloys based on tensile tests, spanning from the supersaturated solid solution to overaged conditions. The initial work hardening rate was seen to decrease with ageing up to the peak-aged condition. Upon overageing it increased again as the particles grew in size and became non- shearable. The transition from shearable to non-shearable precipitates was correlated to a very low hardening rate at the end of the tensile test, a behaviour also observed by Barlat and Vasudevan [34] in AA7075. One limitation of tensile tests is the fact that peak- and overaged samples have low ductility, only a few percent. In order to fully understand the work hardening and deformation mechanisms, it is necessary to study the behaviour up to larger strains and methods other than tensile tests should be used. A few results from large strain experiments on various alloy systems may be found in the literature, and they essentially report the same trend, namely a decreasing work hardening rate with increasing ageing. Gracio et al. [35] performed shear tests on a number of conditions of AA6022, and Lloyd and Kenny [18] torsion tested the alloys AA2036 and AA7010 in their T4 and T6 tempers. Westermann et al. [31-33] looked at 7xxx alloys, and Campbell et al. [36] performed hydraulic bulge tests on an AA6010 alloy and found a very low work hardening rate in the strain range ε=0.1-0.5 in the overaged specimen.

In this paper the initial microstructures of several tempers of AA6063 and AA6082, are studied. The microstructure after plastic deformation is investigated for three different tempers of AA6082 in terms of precipitate structures, dislocation structures and stress-strain behaviour. An attempt to model the work hardening behaviour of the same two alloys is reported in [37].
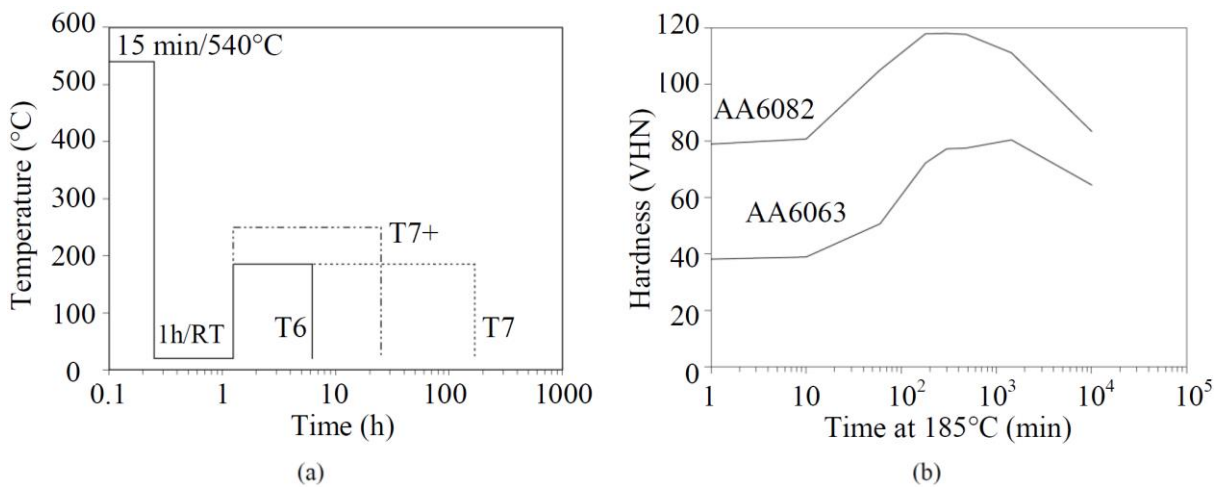
Figure 1: (a) Heat-treatment schedule for the conditions investigated in this report. (b) Hardness as a function of isothermal annealing time at 185°C after 1h/RT.

Table 1. Nominal (and effective) alloy composition of AA6063 and AA6082 (wt%/at%).

Alloy	Mg	Si	Fe	Mn	Cu	eff. Si
AA6063	0.46/ 0.51	0.44/ 0.42	0.19/ 0.09	0.03/ 0.015	0.006/ 0.003	0.38/ 0.36
AA6082	0.67/ 0.74	1.04/ 1.00	0.20/ 0.10	0.54/ 0.27	0.003/ 0.0015	0.79/ 0.76

2. Material and experimental procedures

DC-cast billets of the commercial Al-Mg-Si alloys AA6063 and AA6082 were chosen in favour of extruded profiles in order to avoid effects from texture and deformation structure, but also because of the possibility to make compression specimens of the materials. The chemical composition of the alloys is given in Table 1. It is known that due to the presence of Fe and Mn, a fraction of the Si will be consumed by primary particles and dispersoids. A rule of thumb says that the effective Si-concentration in solid solution in the matrix after casting is reduced to:

$$\left[Si\right]_{eff} = \left[Si\right]_{nom} - \tfrac{1}{3}\left(\left[Fe\right]+\left[Mn\right]\right) \qquad (3)$$

where [X] is the concentration of element X in weight percent. The effective Si-concentration in solid solution is also given in Table 1. The alloys had coarse, equiaxed grain structure (grain size of the order 80-100 μm) and were expected to be texture-free. The billets were homogenised by slow heating (200°C/h) to 580°C, where they were held for 3 h before slow cooling (350°C/h).

The heat-treatment procedure following homogenisation is illustrated in figure 1(a). The alloys were solution heat-treated at 540°C for 15 minutes, quenched, stored at room temperature for one hour and isothermally annealed at 185°C. In figure 1(b) the variation in hardness with ageing time at 185°C is shown. The precipitate structure was studied in the tempers T6, which is the peak strength condition (5h/185°C) and T7, which is overaged (1 week/185°C). In addition, a severely overaged condition of AA6082, called T7+ (24h/250°C), was processed and investigated.

Investigations of the microstructure were performed using a Philips CM-30 transmission electron microscope operating at 150 kV. A Gatan EELS spectrometer was used to measure the foil thickness with an estimated accuracy of 9%. Precipitates were studied with the incident beam parallel to an <001>-direction in the matrix, while the dispersoids were best viewed when tilted out of any zone axis. The size and number of particles were measured on photographic plates. The number density of dispersoids, N_d, was calculated by counting the number, N, over a given area, A, of a specimen of thickness, t:

$$N_d = N \Big/ A\left(t+\overline{d}\right) \qquad (4)$$

where $\overline{d}$ is the average diameter of the dispersoids. The term in the parantheses is a correction for the fact that some of the particles were larger than the foil thickness. As the dispersoids generally appeared to be somewhat elongated, a maximum and minimum diameter were measured on each particle. By approximating them to spheres, a volume fraction, f_d, could be calculated:

$$f_d = N_d \tfrac{4}{3}\pi\left(\tfrac{1}{2}\overline{d}\right)^{3} \qquad (5)$$

A similar procedure was used to determine the number density of precipitates, N_p:

$$N_p = 3N \Big/ A\left(t+\overline{l}\right) \qquad (6)$$

Since the precipitates were needles or rods oriented along the three <100>-directions in the Al- matrix, they appeared as streaks and dots in the TEM. Only the precipitates imaged end-on (dots) were counted (N), as these were the easiest to count. By assuming that they were randomly distributed in three directions, N was multiplied by 3. In order to correct for particles extending out of the foil, the average length, $\overline{l}$, of the precipitates was added to the foil thickness. The volume fraction, f_p, could then be calculated:

$$f_p = N_p \cdot \overline{l} \cdot \overline{A}_p \qquad (7)$$

where $\overline{A}_p$ is the average cross-sectional area of the needles/rods.

Tensile testing was performed on flat specimens (thickness 3mm) in an Instron testing machine, or round specimens (diameter 6 mm) on an MTS machine. Some tests were interrupted at strain levels of 1, 2 and 5%. Uniaxial compression tests of circular specimens (diameter 10 mm) were carried out on a Gleeble machine. A strain rate of 0.1s^{-1} was used in the Instron and Gleeble machines, while the strain rate in the MTS was 0.01s^{-1}. Additionally, the T6 and T7 conditions of AA6082 were cold rolled to large strains. Tensile specimens were cut from the rolled sheets and tested at a strain rate of 0.01s^{-1}.

The T7-curves had an inflection point around ε=0.5, from which it is suspected that some friction effects arise at the highest strains. Therefore, only results up to a strain of ε=0.4 are considered in this

report. A second problem with measuring the strain based on tool movements in the compression tests is the low apparent E-modulus as compared to the tensile tests. This obvious error, which is caused by elastic compression of the tools, is corrected for by applying the following expressions:

$$\varepsilon = \ln\left(\exp(\varepsilon') - \frac{\sigma'}{E'\exp(\varepsilon')}\right) \tag{8}$$

$$\sigma = \sigma'\exp(\varepsilon - \varepsilon') \tag{9}$$

where ε', σ' and E' are the strain, stress and E-modulus measured in the compression test.

In order to study the evolution in deformation structure with strain, three tempers of the AA6082 alloy were examined: W60: Solution heat-treated at 540°C for 15 minutes, quenched and stored at room temperature for one hour before deformation. T6: as W60, but annealed at 185°C for 5h before deformation. T7: as W60, but annealed at 185°C for 1 week before deformation. The strain levels at which the microstructural examination could be carried out, were determined by the tests performed. Fractured tensile specimens were studied, assuming that the strain outside of the neck equalled the uniform elongation of the specimen. For W60 this strain was ε=0.17, while it was only ε=0.05 for T6 and T7. The compression tests were stopped at a strain of about ε =0.8. Since the deformation of compression specimens generally is not homogeneous, they were examined in the middle, i.e. where the effective strain is highest (somewhat higher than the global strain). Both SEM and TEM were used to investigate the microstructure of the deformed materials. Bulk specimens for SEM were prepared by mechanical grinding and polishing, followed by a careful electro polishing (90s/12V) in a methanol-nitric acid solution at -30°C. A Hitachi S-4300SE field emission SEM was used.

Thin foils for TEM were prepared by electrolytical jet-polishing in a methanol-nitric acid solution at -30°C. A Philips CM-30 instrument operating at 150 kV, equipped with a Gatan EELS spectrometer, was used in most of the microstructure investigations. In addition a JEOL JEM-2010 (160 kV) was used. Estimates of the dislocation density were made by counting dislocations (N) intersecting a specified line length (l) on micrographs, taken at positions of known foil thickness (t):
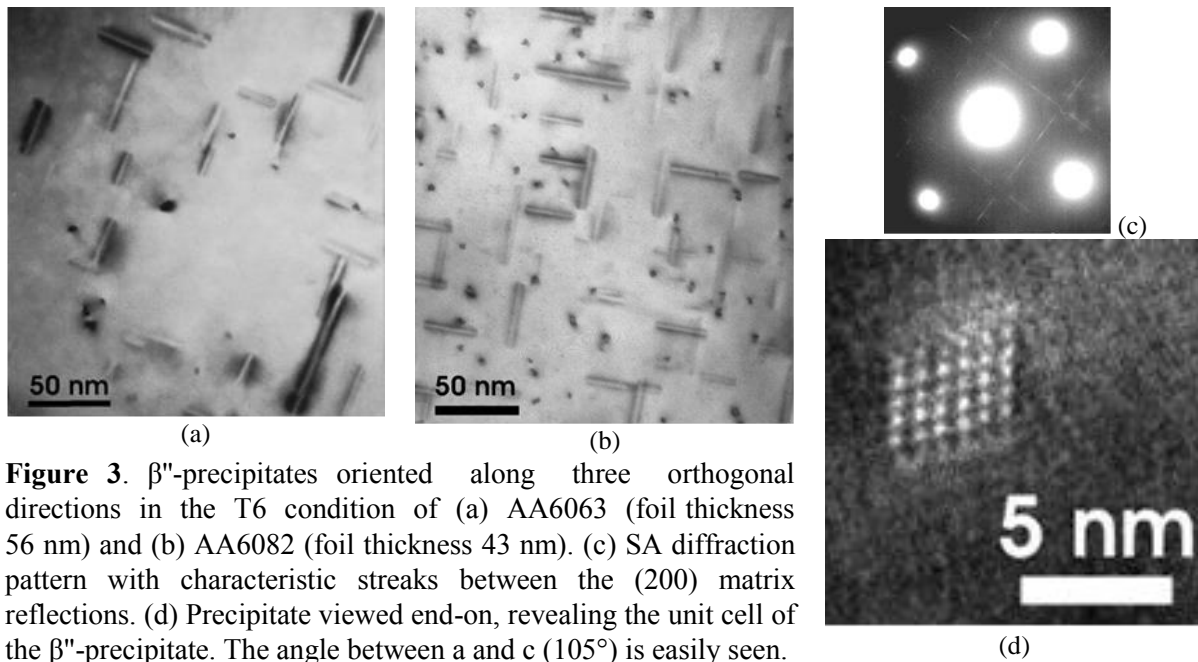
$$\rho = C_1 C_2 N / t l \tag{10}$$

where C_1 is a visibility factor (1 for low-index zone axes, except 1.1 for <110>) and C_2 is a stereological factor, in this case 2 [38].

Table 2. Analysis of the dispersoid structure in AA6082.

Mean radius	80 nm
Aspect ratio	1.9
Number density (N_d)	3.3×10^{18} /m3
Volume fraction (f_d)	1.2 %
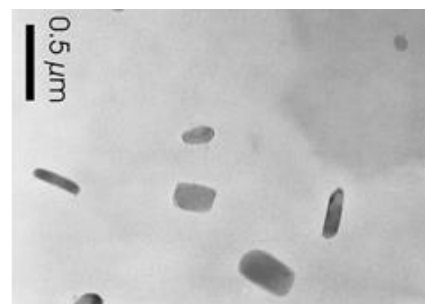
Figure 2. Dispersoids in AA6082.

Figure 3. β"-precipitates oriented along three orthogonal directions in the T6 condition of (a) AA6063 (foil thickness 56 nm) and (b) AA6082 (foil thickness 43 nm). (c) SA diffraction pattern with characteristic streaks between the (200) matrix reflections. (d) Precipitate viewed end-on, revealing the unit cell of the β"-precipitate. The angle between a and c (105°) is easily seen.

Table 3. Analysis of the precipitate structures in AA6063.

	As quenched	T6
Number density (N_p)	-	7.91 x10^{21} /m^3
Volume fraction (f_p)	-	0.30 %
Length	-	32.1 nm
Cross-section area	-	11.9 nm^2
Cross-section aspect ratio	-	1.5
Equivalent cylinder radius	-	1.95 nm
Equivalent sphere radius	-	4.5 nm
Mg in solid solution	0.51 at%[1]	0.40 at%
Si in solid solution	0.36 at%[1]	0.21 t%

[1]Not measured, but taken from the nominal and effective composition, see above

Table 4. Analysis of the precipitate structures in AA6082.

	As quenched	T6	T7	T7+
Number density (N_p)	-	4.26 x10^{22} /m^3	1.04 x10^{21} /m^3	-
Volume fraction (f_p)	-	0.83 %	1.71 %	-
Length	-	28.8 nm	296 nm	0.2-3μm
Cross-section area	-	6.8 nm^2	55.6 nm^2	-
Cross-section aspect ratio	-	1.5	2.1	-
Equivalent cylinder radius	-	1.1 nm	4.2 nm	7-75 nm
Equivalent sphere radius	-	3.6 nm	15.8 nm	-
Mg in solid solution	0.51 at%[1]	0.44 at%	-	-
Si in solid solution	0.36 at%[1]	0.34 at%	-	-

[1]Not measured, but taken from the nominal and effective composition, see above

3. Microstructure

3.1 Dispersoids

Due to the presence of Mn in AA6082, this alloy contains small dispersoids after homogenisation that are stable during later processing. According to the phase diagram, Al6Mn particles are formed in a binary system, but as both Fe and Si are present the particles have more complicated stoichiometries with various amounts of Al, Mn, Fe and Si.

A micrograph of dispersoids is shown in figure 2. In total 140 dispersoids were counted and measured, and the number density and volume fraction determined using equations (4)-(5). The results are summarised in Table 2. No distinction was made between primary particles and dispersoids, as the density of primary particles was expected to be much lower than the dispersoid density and barely contributes to the average values.

3.2 Precipitate structure in peak aged (T6) condition

TEM micrographs of the peak aged condition (5h/ 185°C) of AA6063 and AA6082 are shown in figure 3. As expected, the alloys contain a high density of small needle-shaped precipitates. A difference in number density between the two alloys is also obvious. The appearance of double-lines confirms that the precipitates are surrounded by a coherency strain field. At least 90% of the precipitates, as the one enlarged in figure 3(d), were identified as β''-precipitates having a unit cell of a=1.516 nm, b=0.405, c=0.674 nm and an angle between a and c of 105.3° [4]. By assuming that all the precipitates are β'' with composition Mg_5Si_6, an estimate is given of the amount of Mg and Si that is left in solid solution. In Table 3 and Table 4 measured and calculated average values according to (6)-(7) are given. It is seen that the number density and volume fraction is much less in AA6063 than in AA6082, but at the same time the cross-section area is significantly larger. The precipitates are not exactly cylindrical, as seen by the cross-section aspect ratio of 1.5 in both alloys. However, the area is converted into an equivalent cylinder radius, of which distributions are shown in figure 4 along with the length distributions (normalised by the average value).
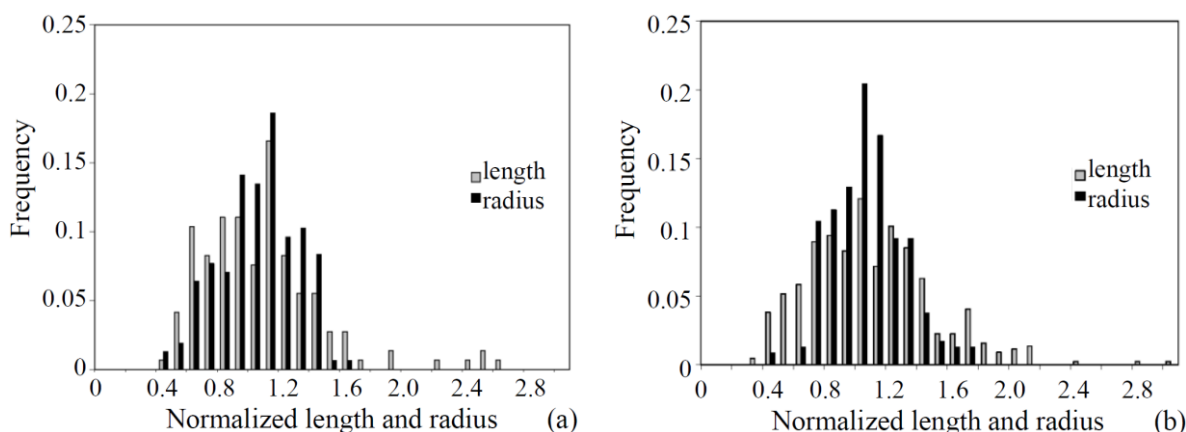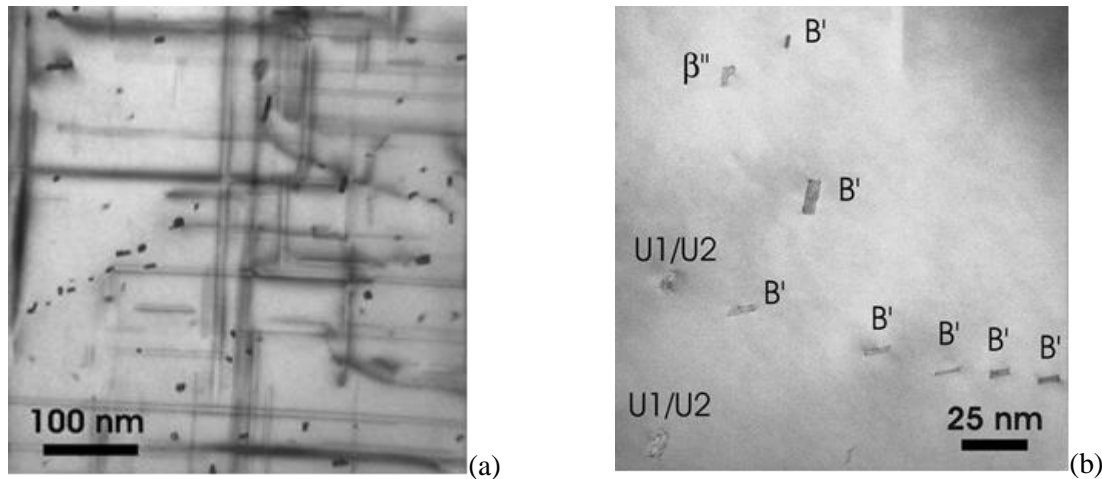

Figure 4. Frequency distributions of length and equivalent cylinder radius, normalised by dividing by the average values, for the T6-condition of (a) AA6063 and (b) AA6082.

3.3 Overaged (T7)

In figure 5 the precipitates in the T7 condition (1 week/ 185°C) of AA6082 are shown. In addition to the obvious increase in cross-section and length, see also Table 4, the size uniformity is much lower than in T6. A larger scatter is seen in the distribution of normalised length and cylinder radius in figure 6, where especially the length distribution has a long tail. The large variation is reflected by the fact that a number of different phases are present. In figure 5(b) the precipitates are identified as β'', B', U1 and U2, but some coarse β'-phases were also observed (not seen on this fine scale). About 60% of the

particles are identified as B', 14% as β'', 10% as U2, while the rest is occupied by U1, β' and some un-identifiable crystal structures. Due to this complexity, and the fact that the composition of B' is not known, it is not possible to estimate the rest of Mg and Si in solid solution. However, because the volume fraction of precipitates is larger than the initial volume fraction of Mg and Si, it is assumed that the rest in solution is close to zero. Another interesting observation is that double-lines, indicating coherency strains, are still present around some of the particles, even though the alloy has been aged for a long time. Note also that obviously some precipitates are formed on dislocations where they appear as pearls on a string. A few dislocations are also seen.

(a)

(b)

Figure 5. (a) Precipitates in AA6082 in the T7 condition, oriented along three orthogonal directions in the matrix. (b) Identified phases.
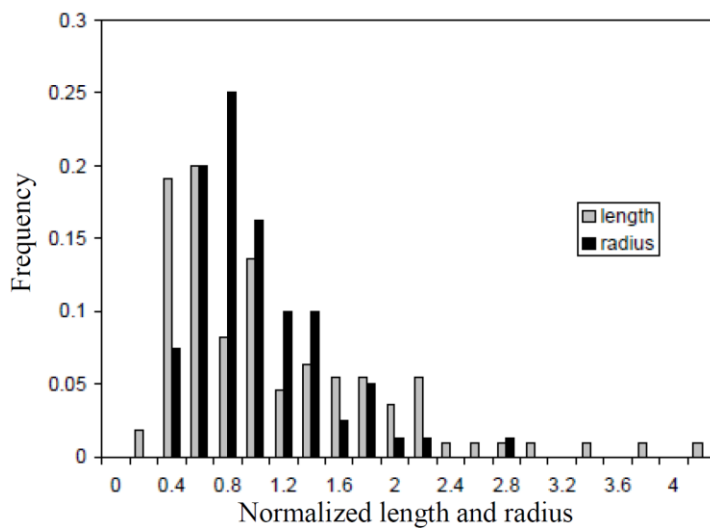
Figure 6. Frequency distributions of length and equivalent cylinder radius, normalised by dividing by the average values, for the T7-condition of AA6082.

(a)

(b)

(c)

d)
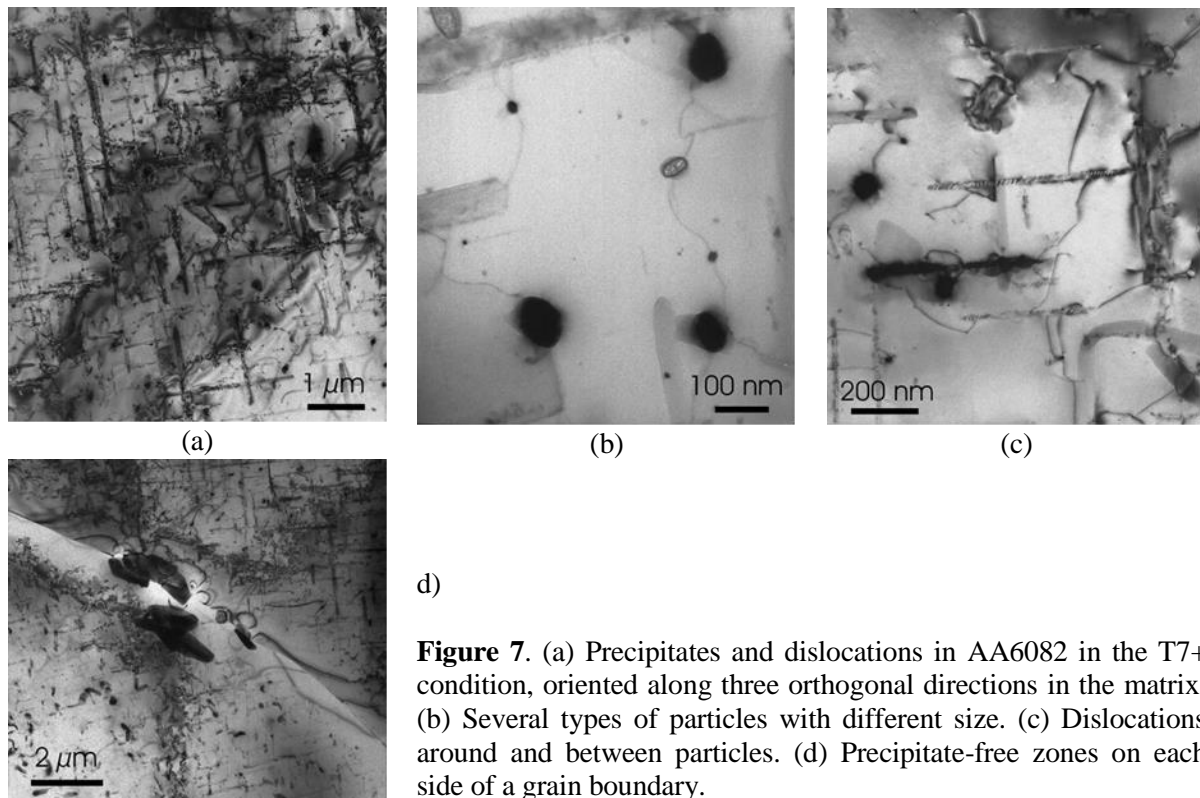
Figure 7. (a) Precipitates and dislocations in AA6082 in the T7+ condition, oriented along three orthogonal directions in the matrix. (b) Several types of particles with different size. (c) Dislocations around and between particles. (d) Precipitate-free zones on each side of a grain boundary.

3.4 Severely overaged (T7+)
In figure 7 micrographs of the severely overaged condition (24h/250°C) of AA6082 are shown. The precipitates seen in figure 7(a), with a close-up in figure 7(b), are very large, with lengths of about 1-3 µm and diameters of 50-150 nm, which suggests that they are U1-precipitates. However, as seen in figure 7(b), there exist two or three particle populations of different size. A set of small particles are measured to have a typical diameter of about 15 nm. These are estimated to be some hundred nm's long. A striking observation in this specimen is the high density of dislocations, figure 7(a, c), despite the fact that it has not been subjected to any external deformation. These dislocations are absent in the precipitate-free zones, see figure 7(d).


(a)

(b)

(c)
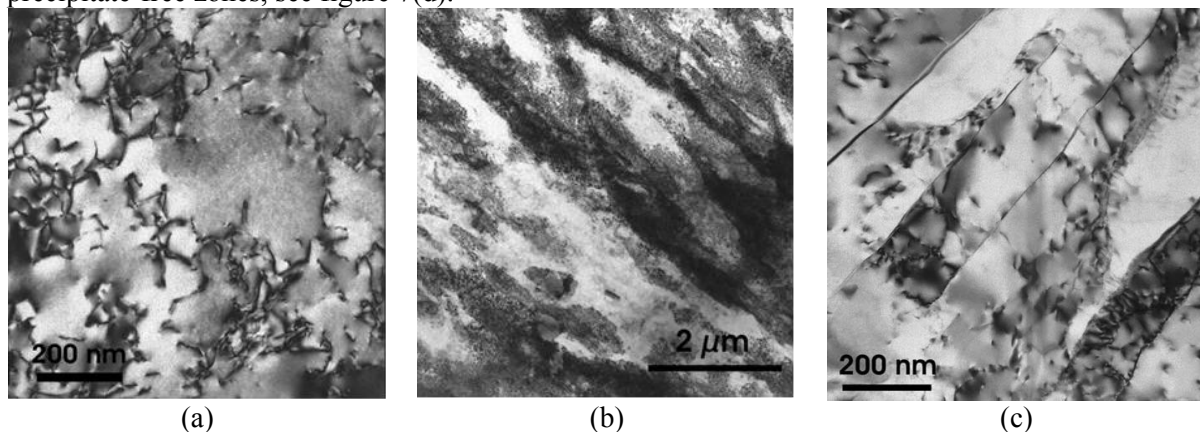
Figure 8. AA6082. Deformation structures in the W60 condition. (a) ε=0.17 (tensile test specimen) (b-c) ε=0.8 (compression test specimen)

3.5 Naturally aged (W60) and deformed AA6082

The W60 condition contains approximately 1.5 at% solute (Mg+Si) which is partially clustered. In general the dislocation structure is seen to be rather diffuse, figure 8. The dislocation density is relatively homogeneous, without any clear cell or subgrain structure. After large deformation the structure is dominated by ragged bands that are probably gradually misorientated to each other, figure 8(b), although some sharper well-defined subgrain boundaries are found as well, figure 8(c).

(a)

(b)

(c)

(d)
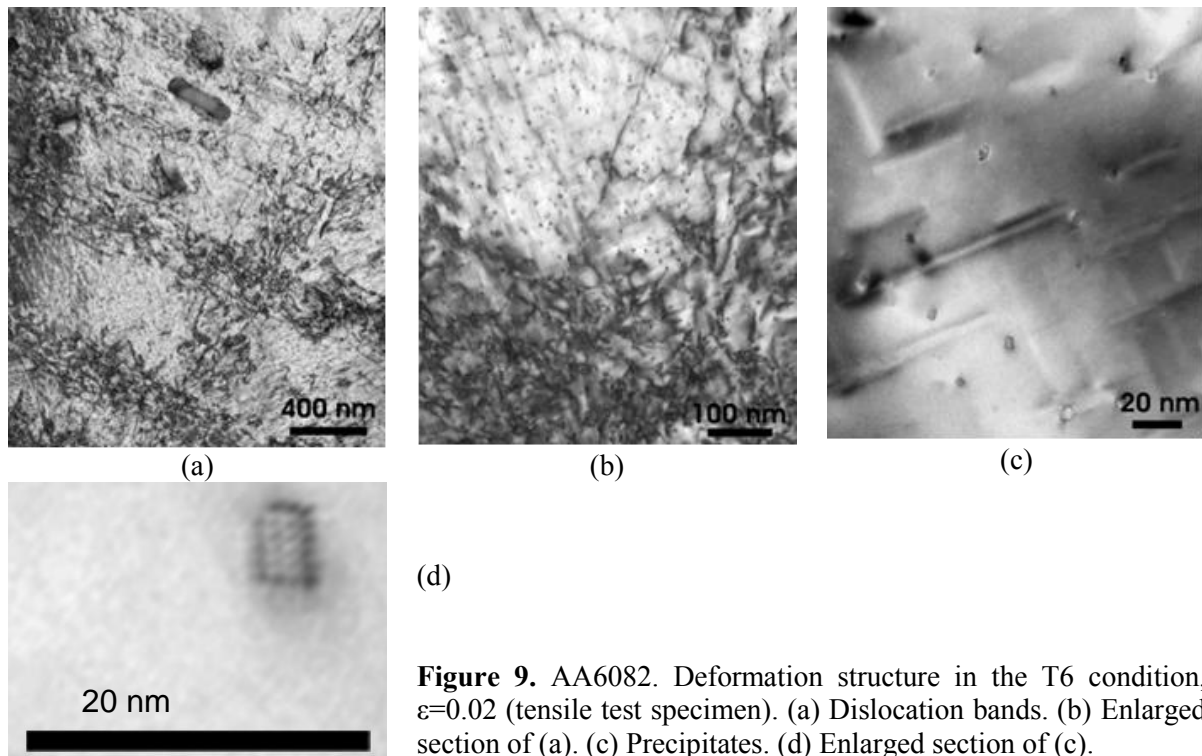
Figure 9. AA6082. Deformation structure in the T6 condition, ε=0.02 (tensile test specimen). (a) Dislocation bands. (b) Enlarged section of (a). (c) Precipitates. (d) Enlarged section of (c).

(a)

(b)

(c)
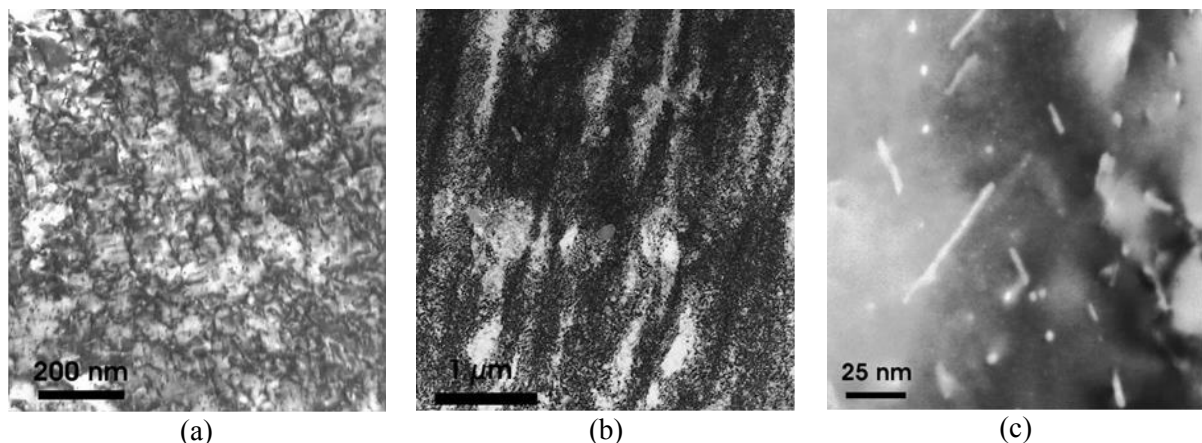
Figure 10. AA6082. Deformation structure in the T6 condition. (a) ε=0.05 (tensile test specimen) (b-c) ε=0.8 (compression test specimen).

3.6 Peak aged (T6) and deformed AA6082

The peak aged condition has a fine dispersion of needle-shaped β" and a solute content of about 0.8 at% (Mg+Si). After 2% plastic straining the dislocations are seen to be localised into bands surrounding cells of low dislocation density and a size of 0.5-1 μm, figure 9(a-b). The bands are crystallographic in nature, in such a way that when they are viewed along an <001> direction, they

form orthogonal bands in the <011> directions. It is therefore most likely that the dislocations lie on parallel {111} planes in the matrix. Such a localisation is often associated with the cutting of precipitates, which is also indicated by the observation of disrupted coherency strain fields, figure 9(c). However, the atomic structure of the precipitates is still clearly visible in figure 9(d).

After 5% straining, these bands have more or less disappeared, and a uniform dislocation structure of a very high density dominates the material, figure 10(a).

(a)   (b)   (c)

(d)
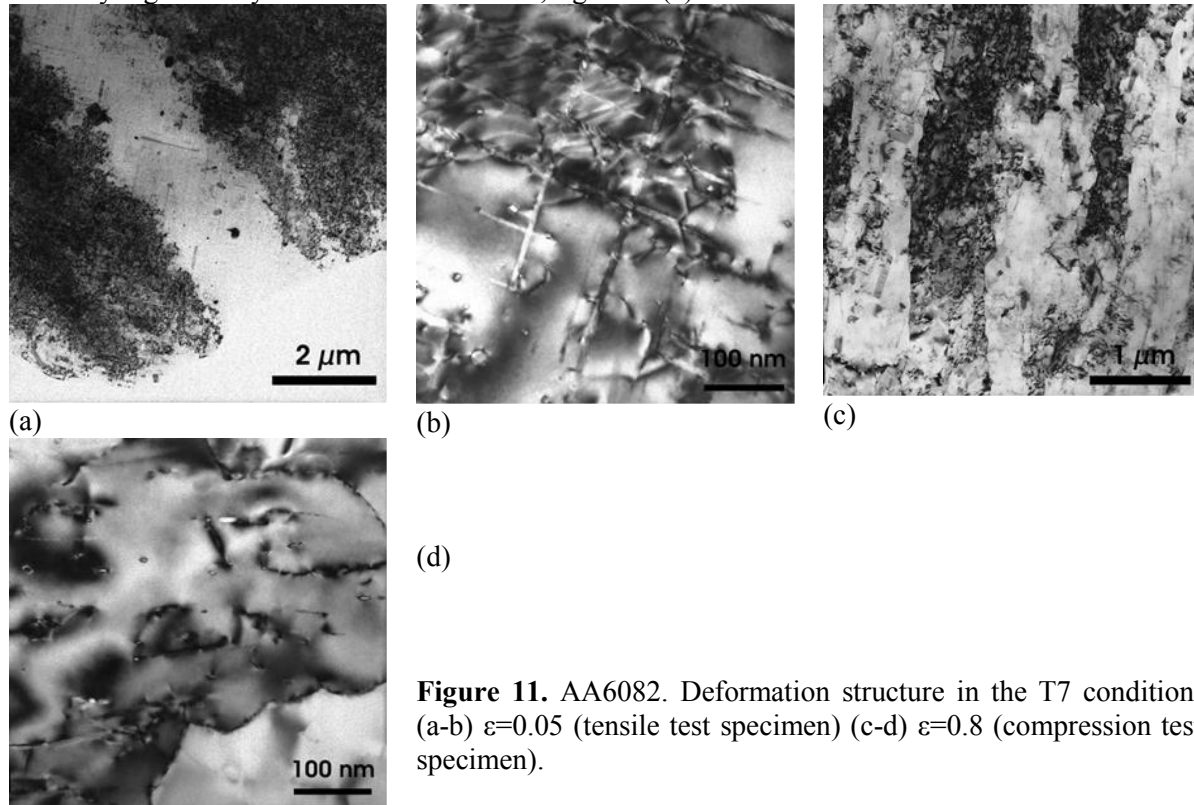
Figure 11. AA6082. Deformation structure in the T7 condition. (a-b) ε=0.05 (tensile test specimen) (c-d) ε=0.8 (compression test specimen).

In the highly deformed material the microstructure resembles that of the W60 condition, i.e. diffuse bands of gradual misorientations, figure 10(b). The precipitates are still visible, but now they create an angle to each other that is different from the initial 90° (in figure 10(c): 60°). Even though some irregularities may be seen, the precipitates are relatively straight. This must imply that the dislocations that cut the precipitates are very homogeneously distributed along one particle.

(a)   (b)   (c)
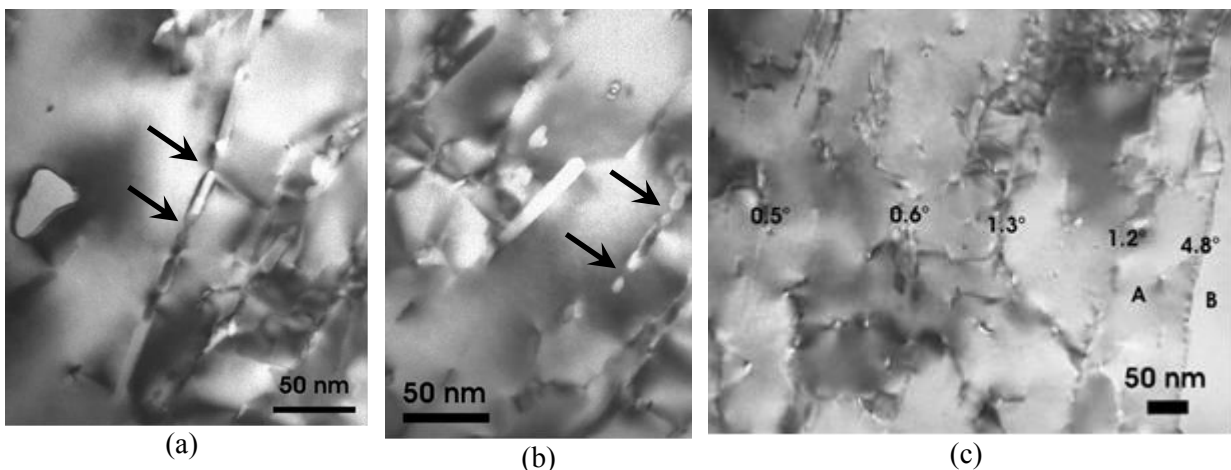
Figure 12. AA6082. Deformation structure in the T7 condition, ε=0.8 (compression test specimen). (a-b) Fragmented precipitates marked with arrows. (c) Measured misorientations across boundaries.

3.7 Overaged (T7) and deformed AA6082

The overaged condition contains a lower density of coarser precipitates than T6, and there is almost no solute left in the matrix. In the early stages of deformation, dislocations are tangled between the precipitates in a rather uniform way, although some dislocation bands were found here as well, figure 11(a-b). At large strains the structure consists of sharp boundaries, figure 11(c), quite different from the diffuse bands in W60 and T6. Obviously, the boundaries have been pinned by the precipitates, as they are sometimes curved into small arcs, figure 11(d). The boundaries separate material volumes of different orientation, similar to the cell block structure that is observed in pure aluminium [21]. Orientation measurements in figure 12(c) show that the misorientation across these boundaries is of the order 3-5°. Within these blocks smaller volume elements can be observed, although they are not as clear as in single-phase materials. Small misorientations (0.5-2°) can be detected across the boundaries.
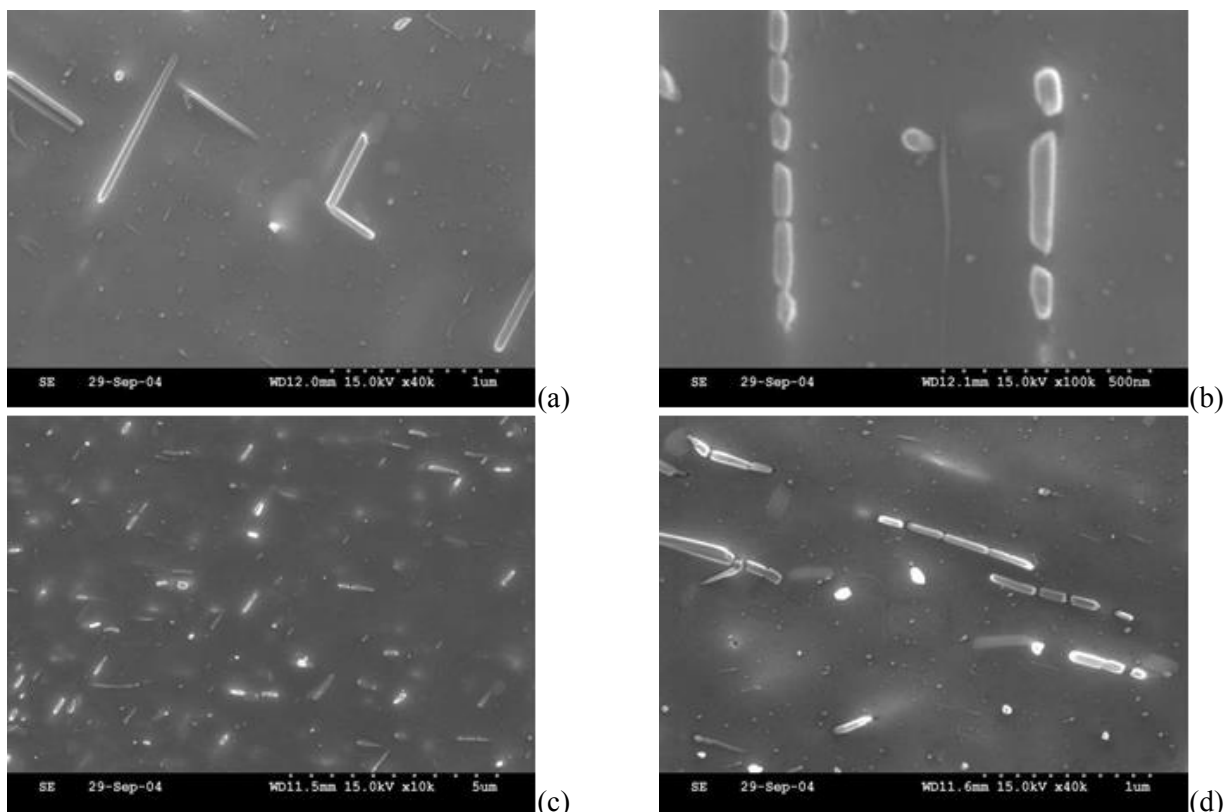

Figure 13. AA6082. SEM micrographs of the T7 condition. (a) Uniform part of tensile test specimen (ε=0.05). (b) Near the fracture surface of the tensile test specimen. (c-d) Compression test specimen (ε=0.8).

When it comes to the precipitates it is seen that they to a large extent are fragmented into smaller pieces, figure 12(a-b). Because of the interface energy between particles and matrix, the fragments are rounded at their ends and in some cases have become spherical. SEM micrographs give information on the population of coarser precipitates in T7. In the uniform region of a tensile test specimen (ε=0.05) the particles are intact, figure 13(a). However, when we move into the neck, figure 13(b), where the local strains have been higher, we see frequent particle fragmentation. Similarly, in the compression tested specimen the particles are broken, figure 13(c-d).

Table 5. Mechanical properties for AA6063 and AA6082

	AA6063				*AA6082*				
	W10	T6x	T6	T7	W5	T6x	T6	T7	T7+
$R_{p0.2}$ (MPa)	36.6	95.6	190.4	165.4	65.0	222.8	321.5	213.8	98.0
R_m (MPa)	121	164.2	222.1	198.7	191.0	299.8	339.5	259.3	172.0
e_u	0.26	0.15	0.082	0.064	0.21	0.13	0.059	0.062	0.072
e_f	0.37	0.25	0.16	0.14	0.30	0.16	0.072	0.11	0.15
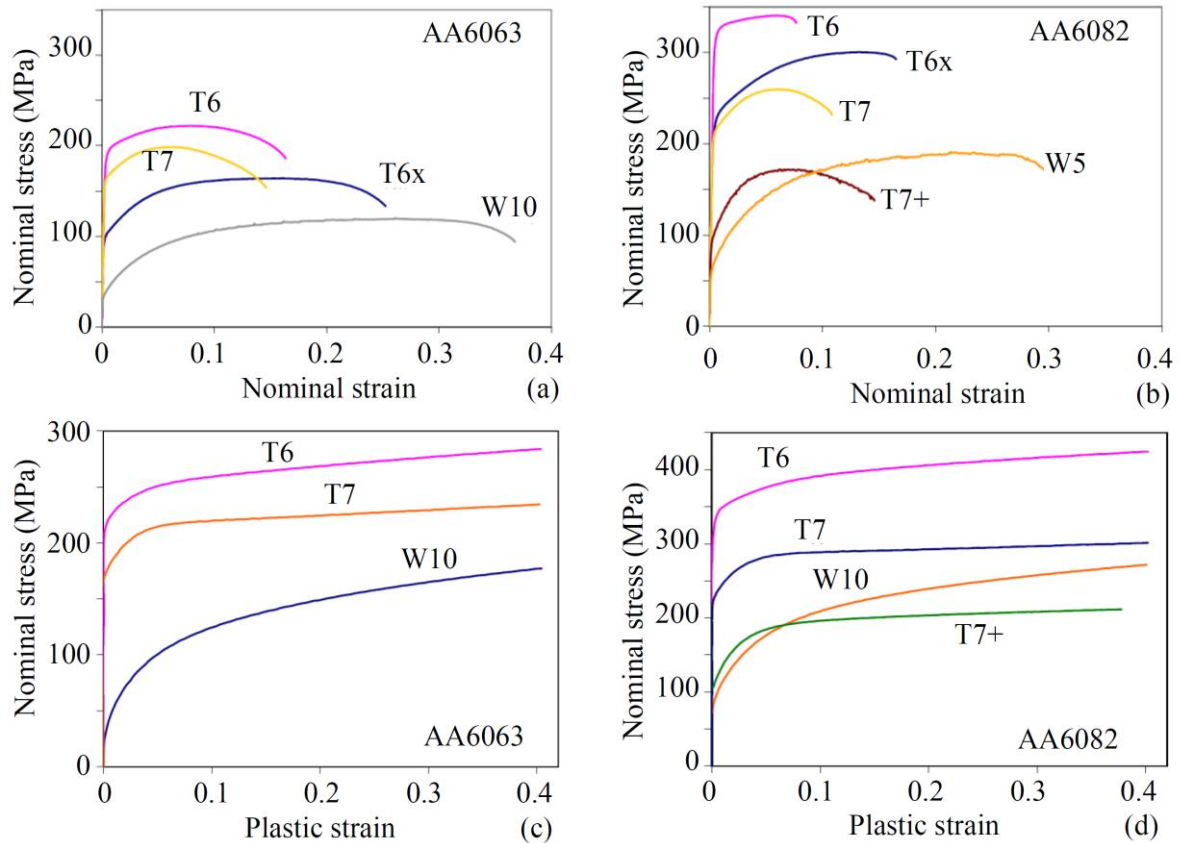
**Figure 14.** Nominal stress-strain curves. (a-b) by tensile tests, (c-d) by compression tests.
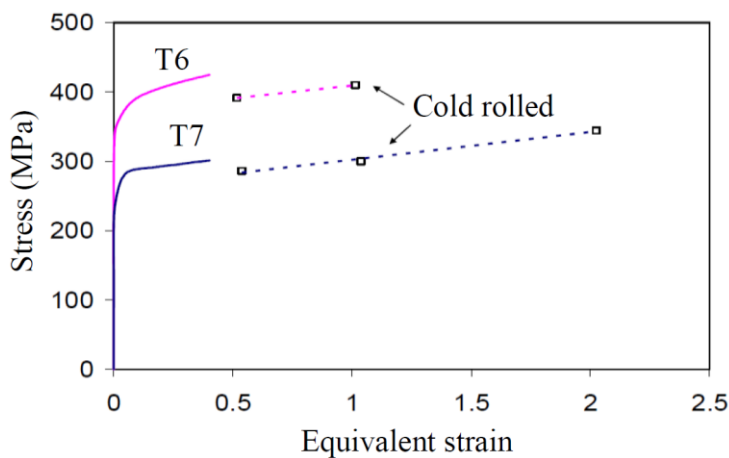
Figure 15. Stress-strain behaviour of AA6082 T6 and T7 obtained from compression tests and cold rolling + tension tests.

4. Mechanical properties

Stress-strain curves by tensile and compression tests of the artificially aged conditions of AA6063 and AA6082 are shown in figure 14 and some properties are listed in Table 5. As expected, the strength ($R_{p0.2}$, R_m) increases and the ductility (e_u, e_f) decreases with ageing from the as-quenched state to T6. During overageing the strength decreases while the uniform elongation remains almost constant. The amount of work hardening (R_m-$R_{p0.2}$) decreases with ageing up to T6, but increases again with overageing. The flow stress from compression tests is plotted according to the strain correction described in (8) and (9). The differences in work hardening behaviour between the tempers are obvious from both the tensile and the compression tests. The compression results essentially give a continuation of the trends from the tensile results. An estimate of the further work hardening, obtained by cold rolling followed by tensile tests, is shown for the conditions T6 and T7 of AA6082 in figure 15.

The post- uniform elongation, as well as the load reduction from maximum load to fracture, are significant in the overaged conditions. This increases the critical failure strain, CFS, (2), but also the higher ductility of the AA6063 alloy has a positive effect on the CFS, see figure 16.
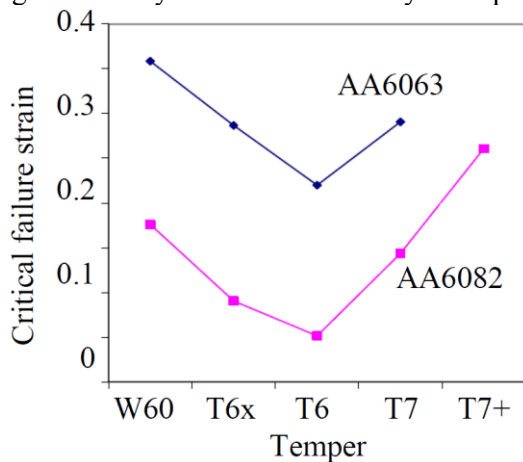
**Figure 16**. Critical failure strain (CFS) of various tempers of the two alloys.

The rate of work hardening, θ, measured in both tension and compression testing, is plotted against the reduced flow stress for each temper in figure 17 and figure 18. The initial work hardening rate is seen to decrease with ageing up to T6, and the subsequent hardening rate decreases gradually for these conditions. The overaged conditions, however, have a higher initial θ than T6, but decrease rapidly to a low and stable θ.
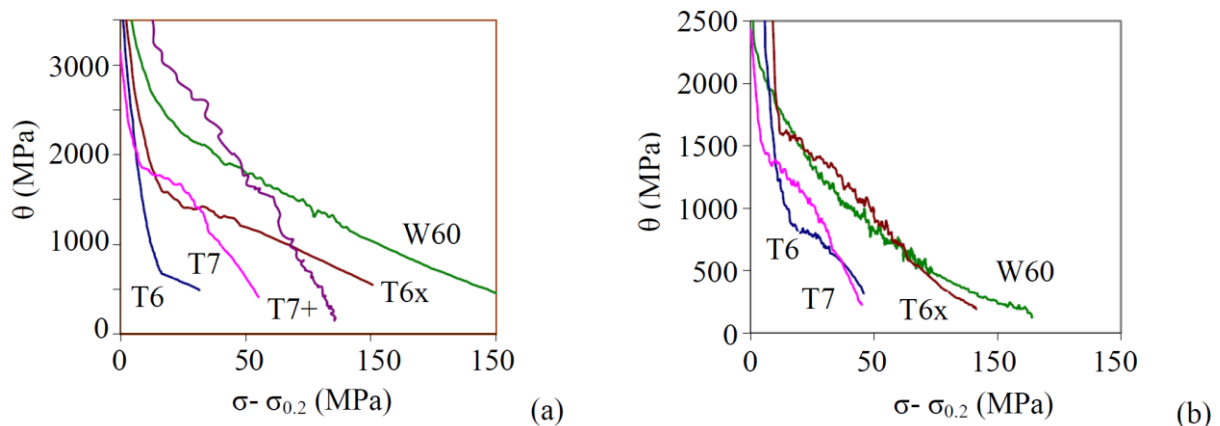
Figure 17. Work hardening rate (θ) as a function of reduced flow stress from tension tests for (a) AA6063 and (b) AA6082.

5. Discussion

The two alloys investigated in this work have a significant difference in composition, as AA6082 contains almost twice as much Mg+Si as AA6063. This alone results in a lower number density and volume fraction of precipitates in AA6063 T6, but it is also responsible for a slower precipitation reaction at room temperature [39]. Therefore, it is reasonable to assume that the number of various Mg and Si containing clusters formed after one hour at room temperature is very different. During ageing at 185°C these clusters act as nucleii for precipitates. Since the number of nuclei is low in AA6063, fewer precipitates will be formed. However, because the spacing of precipitates is larger they can grow faster than in AA6082. This may explain the differences seen in figure 3, Table 3 and Table 4. According to the measurements the amount of Mg and Si in solid solution is reduced by about 50% from the as-quenched state to T6 in AA6082. In AA6063 the reduction is only 30%.
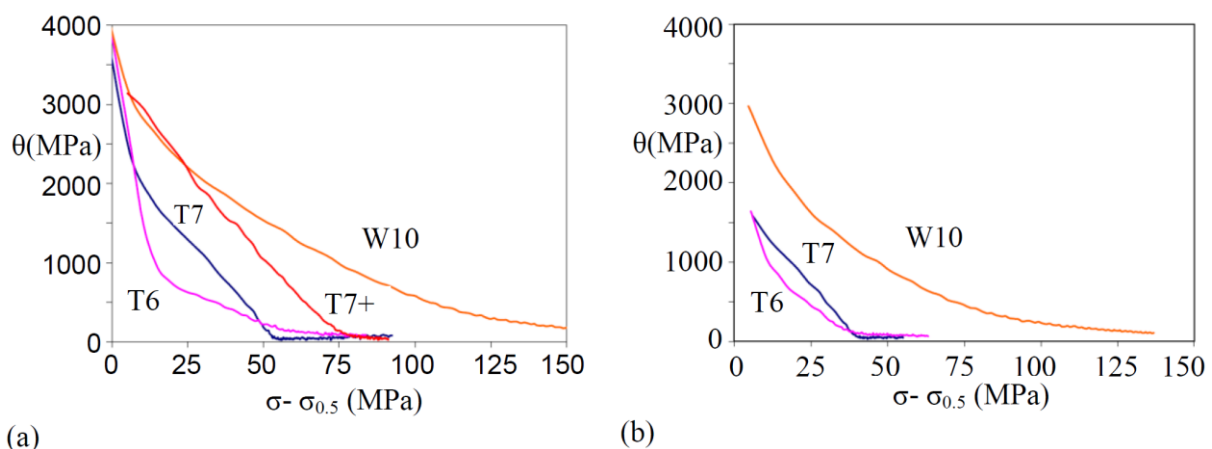
Figure 18. Work hardening rate (θ) as a function of reduced flow stress from compression tests for (a) AA6063 and (b) AA6082.

As expected, the T6 condition contains a high density of β''-precipitates. No underaged conditions have been investigated in this work, but based on the work by e.g. Marioara et al. [3] it is a reasonable assumption that GP-zones would be found after shorter ageing times.

With further annealing the matrix becomes essentially depleted of solutes, giving a volume fraction of particles that is in fact higher than the original volume fraction of solutes. This is possible, since some of the precipitates contain Al in addition to Mg and Si. Giving a statistical analysis of the particle size, number density and volume fraction becomes increasingly difficult with increased overageing, as the uniformity of the particles is worsened. The high dislocation density in T7+ makes it even more difficult to measure the particles. However, several metastable phases are seen, while no evidence of the equilibrium phase β or Si-particles is found. An ageing temperature of 185°, and even 250°C, has probably been too low for these phases to be formed. It can be concluded that the overageing is quite slow at 185°C, and the presence of coherency strains around the particles in T7 confirms this.

The presence of dislocations arranged around and between the particles in the overaged conditions is worth an extra comment. First of all, it is realized that they must originate from some late stage of the sample preparation, as a majority of the dislocations would have been annealed out during ageing. Therefore the final quench as well as the thin foil preparation and handling are the only possibilities. But since all the dislocations are arranged around and between the particles and none of them in the precipitate-free zones, we can eliminate artefacts from bending of the foil or similar deformation. In the severely overaged sample (T7+) the precipitates are assumed to be incoherent with the matrix. This implies that during the precipitation reaction dislocations must be formed on the interface already before quenching. During cooling the different coefficients of thermal expansion between particles and matrix lead to a difference in volume contraction, and the forces arising may punch dislocations

away from the interface. Especially in the T7+ sample, which is quenched from 250°C, large thermally-induced strains can be expected. In the T7 sample this occurs to a much lesser extent, as many of the precipitates are still coherent. The presence of thermally-induced plastic zones is a well-known phenomenon in metal-matrix composites, and local strains of the order 1%, evidenced by slip bands, have for example been observed in the neighborhood of cylinder-shaped SiC-particles [7].

In the peak aged condition, T6, a localization of dislocations into bands at 2% strain indicates that the precipitates are shearable. The disappearance of the bands at higher strain is in accordance with Dowling and Martin [20], who interpreted this as an effect of dispersoids spreading the slip. The bands seen in the compressed specimen, i.e. ε=0.8, are not crystallographic in the same way as at low strains. At ε=0.8 the needle-shaped precipitates are sheared uniformly by dislocations so that they remain straight needles but not in the <001> directions anymore. This indicates extensive cross slip.

In the overaged specimen, T7, it is seen that the low solute content in the matrix gives a "cleaner" dislocation structure. The dislocations have been able to recover and reorganize into sharp boundaries. Above some critical strain the precipitates are fragmented. The SEM micrographs indicate that for the coarsest precipitates this critical strain is somewhere above 5% strain. The smallest precipitates can probably accommodate larger elastic strains, and have therefore undergone some bending before they also fracture, as in the compressed sample.

Generally, it is seen from the results above that AA6063 is softer and more ductile than AA6082, and that the ageing response is faster and stronger in AA6082. This is reasonable, as the AA6082 alloy has a considerably higher amount of Mg and Si, giving more solution hardening and a higher precipitation rate. But it is also seen that the ageing results in a number of effects on the mechanical properties, and in the following a more detailed discussion is given on the behaviour of the different conditions.

A comparison of the as-quenched states of the current alloys, i.e. AA6063 W10 and AA6082 W5, with other solid solution alloys [10] reveals something interesting, see figure 19. The AA6063 alloy, having 0.51 at% Mg and 0.36 at% Si, in total 0.87 at% in solid solution, has a stress-strain curve which is practically identical to an alloy containing 1.1 at% Mg. The AA6082 alloy with 1.5 at% Mg+Si has an identical behaviour as an alloy with 3.2 at% Mg. AA6082 contains a considerable amount of dispersoids that must account for a fraction of the strength. Anyway, from the high hardening rate it is apparent that the effect of having Mg and Si in combination is larger than having only Mg. Such a synergistic effect is also observed by others [40, 41].

However, this must also be viewed in light of what happens to the alloys after only short storage times at room temperature caused by atomic clusters [1], and it is easy to imagine that the formation of such clusters may be accelerated by deformation, i.e. dynamic precipitation, a well-known phenomenon in age-hardenable alloys [42, 43]. Hence, it is possible that the synergistic effect of Mg and Si may be related to the enhanced clustering due to deformation.
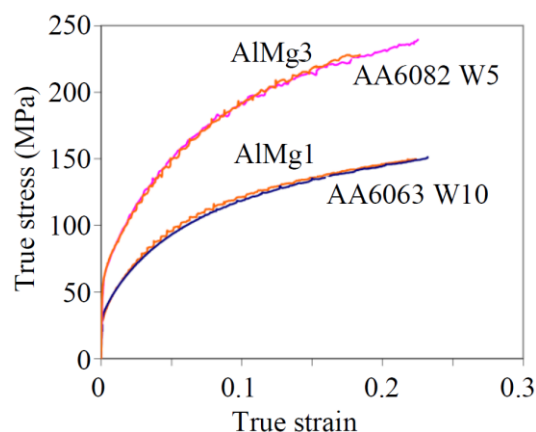
Figure 19. Comparison of tensile tests of AA6063 W10 with AlMg1, and AA6082 W5 with AlMg3.

The increase in yield strength that occurs during ageing up to 5h/185°C is caused by the high density of small, coherent β"-precipitates. Such precipitates are generally considered as shearable, and it has been claimed that they do not contribute to the work hardening, which then is defined solely by the matrix properties [44]. This idea is complicated by the observation of a gradual elastic-plastic transition in the T6-samples of both AA6063 and AA6082, giving a very high work hardening rate immediately after the yield point. Lloyd and Kenny [18] explained this by suggesting that the precipitates are non-shearable at the early stage of deformation, leaving Orowan loops around them. The back stress arising from the dislocation loops will be relieved upon further deformation when the dislocations start cutting through the precipitates. The barrier strength is then reduced and the work hardening rate decreases.

The reduction in number density of precipitates during overageing as well as the loss of coherency, are probably responsible for the reduction in yield strength in T7 and T7+. Additionally, the strain field around precipitates in Al-Mg-Si alloys have been observed to be much stronger if they are rod-shaped than if they are laths [45]. It was seen that the T7-condition of AA6082 contained a large number of lath-shaped B'-precipitates, while the β" in T6 had a more circular cross-section. Hence, the B'-precipitates will contribute less to the strength than the β"-precipitates do, even if they are of similar size. This may cause an extra reduction in yield strength of T7.

A factor of significant importance when deforming two-phase materials is the accumulation of internal back stresses arising from elastic deformation of a second-phase surrounded by a plastically deformed matrix. The back stresses may be evidenced by observations of aided reverse flow, e.g. non-linear unloading or the Bauschinger effect. The theoretical framework was established by Brown and Stobbs [46], and later it has been argued that the stresses can be responsible for large strengths [47]. Since the back stress saturates it does not contribute to the work hardening rate. The cracking of precipitates in the overaged conditions reduces the back stress and softens the material. In this work, however, reverse tests have not been performed to quantify this phenomenon.

The shape of the work hardening curves obtained from tensile tests in figure 17 is analysed using the method described by Cheng et al. [30]. Two parameters, the initial work hardening rate θ_{max} and the rate of decrease of the hardening rate $d\theta/d\sigma$, are read from the curves and plotted as a function of the yield strength in figure 20. Firstly, it is recognised that θ_{max} decreases linearly with the yield strength up to T6, but increases with $\sigma_{0.2}$ at a faster rate in the overaged conditions, figure 20(a,c). The highest initial work hardening rate is found in the condition with the lowest yield strength, and vice versa. Secondly, the rate of decrease of the hardening rate is almost unaffected by the ageing up to T6 (except AA6063 T6, see below), while overageing gives a much more rapid decrease, figure 20(b,d). The observations are in accordance with the ones made by Cheng et al. [30]. They associated θ_{max} to the storage rate of dislocations. The parameter $d\theta/d\sigma$ they linked to the dynamic recovery rate. The dramatic difference between underaged and overaged conditions could then be interpreted as an effect of the transition from shearable to non-shearable particles.

A comparison of the overaged conditions T7 of AA6063 and AA6082 with a commercially pure aluminium alloy is shown in figure 21. The flow stress of the AA1050 alloy is obtained by compression testing to a strain of $\varepsilon=0.5$, and by cold rolling followed by tensile testing at larger strains [48]. It can be seen that the work hardening rate at $\varepsilon>0.1$ in the overaged materials, see also figure 14 and figure 15, is of the same order as that observed in stage IV of work hardening observed in AA1050. This may indicate that the overaged conditions of the 6xxx alloys have reached a stage IV at a much smaller strain than AA1050. The onset of stage IV of an AA1050-type alloy is at a strain of about $\varepsilon=0.7$. The stage is characterised by continued hardening due to decreasing boundary spacing, and a dislocation density in the subgrain interior that, because of dynamic recovery, has saturated at the end of stage III [47].
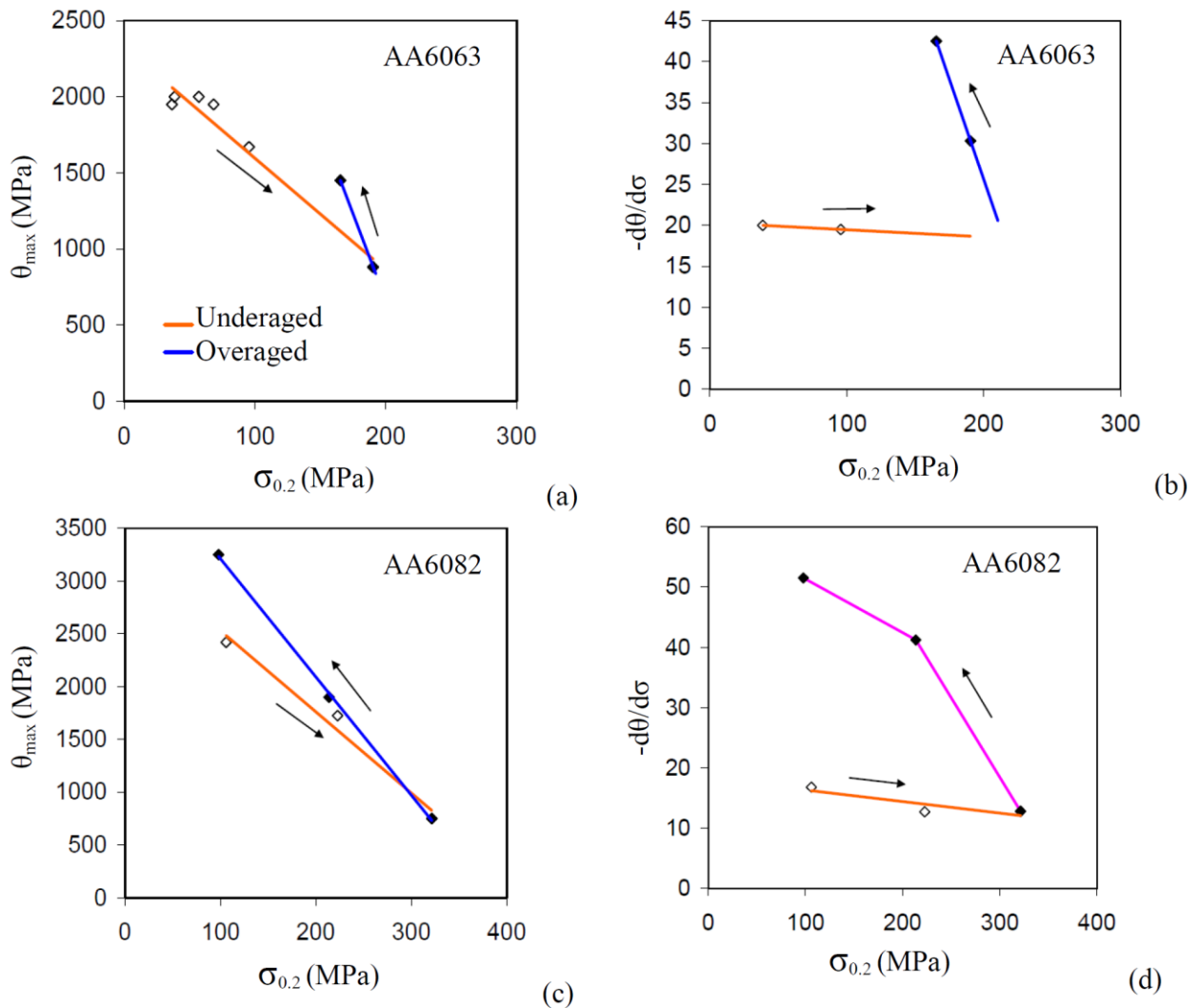
Figure 20. The initial work hardening rate, θ_{max}, and the rate of decrease of the hardening rate, $d\theta/d\sigma$, plotted as a function of the yield strength. Open symbols: underaged conditions, closed symbols: peak aged and overaged conditions. In (a) also the naturally aged conditions are plotted.
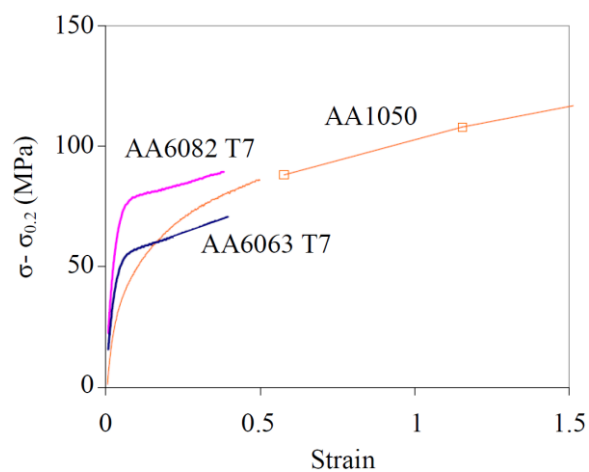
Figure 21. A comparison of the reduced flow stress between AA1050 and the overaged conditions of AA6063 and AA6082.

6. Conclusions

The precipitate structures and corresponding work hardening behaviour in AA6063 and AA6082 have been characterized by TEM and investigated by tensile and compression testing. In the as quenched condition the dislocation structure of the AA6082 is diffuse at small strains. At larger strains ragged bands and subgrains are gradually misoriented to each other. In the T6 condition a dislocation cell structure is recognised at 2% strain but has been replaced by a more homogenous distribution of dislocations at 5% strain. During 80% deformation the needle-shaped precipitates are sheared uniformly by dislocations so that they remain "straight needles" but not with <001>-orientations anymore. This indicates extensive cross slip. At larger strains a subgrain structure is observed. In the overaged conditions dislocations are present surrounding the coarse precipitates in the initial material being formed during the ageing treatment, most likely during quenching. More dislocations are tangled between the coarse precipitates at low strains, whereas a subgrain structure is formed at the larger strains. Cracking of the largest precipitates are observed at large strains in the T7 and T7+ conditions.

The Mg and Si interact and cause a strong work hardening in the as quenched condition, similar to AlMg alloys with about twice as much alloying elements (Mg+Si) in solid solution. It is found that the initial rate of work hardening is lowest at T6, whereas the work hardening rate at slightly larger strains keeps decreasing with increased aging times. In T7 the work hardening rate is similar as if the alloy went straight into stage IV subsequent to the initial. At long aging time large precipitates break and reduce the work hardening rate further. The critical failure strain reaches a minimum in the peak aged conditions.

References

[1]   Edwards G A, Stiller K, Dunlop G L and Couper M J 1998 *Acta Mater*. **46** 3893-3904
[2]   Murayama M and Hono K 1999 *Acta Mater*. 47 1537-1548
[3]   Marioara C D, Andersen S J, Jansen J and Zandbergen H W 2001 *Acta Mater*. **49** 321-328
[4]   Andersen S J, Zandbergen H W, Jansen J, Traeholt C, Tundal U and Reiso O 1998 *Acta Mater*. **46** 3283-3298
[5]   Marioara C D, Andersen S J, Royset J, Reiso O, Gulbrandsen-Dahl S, Nicolaisen T E, Opheim I E, Helgaker J F and Holmestad R 2014 *Metall. Mater. Trans. A* **45A** 2938-2949
[6]   Perovic A, Perovic D D, Weatherly G C and Lloyd D J 1999 *Scripta Mater*. **41** 703-708
[7]   Ashby M F 1970 *Philos. Mag*. **21** 399
[8]   Brown L M and Ham R K 1971 *Dislocation-particle interactions*, in: A. Kelly, R.B. Nicholson (Eds.) Strengthening Methods in Crystals, Elsevier, Amsterdam, 1971, pp. 9-135
[9]   Ardell A J 1985 *Metall. Trans. A* **16** 2131-2165
[10]   Humphreys F J and Hatherley M 1996 *Recrystallization and related annealing phenomena*, Pergamon, Oxford.
[11]   Bay B, Hansen N, Hughes D A and Kuhlmannwilsdorf D 1992 *Acta Metall. Mater*. **40** 205-219
[12]   Bay B, Hansen N and Kuhlmannwilsdorf D 1992 *Mat. Sci. Eng*. **158** 139-146
[13]   Hughes D A 1993 *Acta Metall. Mater*. **41** 1421-1430
[14]   Korbel A, Embury J D, Hatherly M, Martin P L and Erbsloh H W 1986 *Acta Metal*. **34** 1999-2009
[15]   Banizs K 1979 *Mater. Sci. Eng*. **41** 17-24
[16]   Zhen L and Kang S B 1997 *Metall. Mater. Trans. A* **28** 1489-1497
[17]   Blankenship C P, Hornbogen E and Starke E A 1993 *Mat. Sci. Eng*. **169** 33-41
[18]   Lloyd D J and Kenny D 1982 *Metall. Trans. A* **13** 1445-1452
[19]   Ryum N, Haegland B and Lindtvei.T 1967 *Z Metallkd* **58** 28-31
[20]   Dowling J M and Martin J W 1976 *Acta Metal*. **24** 1147-1153
[21]   Vivas M, Lours P, Levaillant C, Couret A, Casanove M J and Coujou A 1997 *Philos. Mag. A* **76** 921-931
[22]   Gutierrez-Urrutia I, Munoz-Morris M A and Morris D G 2005 *Mat. Sci. Eng*. **394** 399-410

[23] Nourbakhsh S and Nutting J 1980 *Acta Metal.* **28** 357-365

[24] Sargent C M and Purdy G R 1974 *Scripta Metall. Mater.* **8** 569-572

[25] Poole W J, Wang X, Lloyd D J and Embury J D 2005 *Philos. Mag.* **85** 3113-3135

[26] Yeh J R, Summe T L and Seksaria D C 1999 in: H.F. Mahmood, S.D. Barbat, M.R. Baccouche (Eds.) Craschworthiness, occupant protection and biomechanics in transportation systems (AMD 237/BED 45), ASME, New York, pp. 97-105

[27] Deschamps A and Brechet Y 1998 *Acta Mater.* **47** 293-305

[28] Esmaeili S, Lloyd D J and Poole W J 2003 *Acta Mater.* **51** 2243-2257

[29] Myhr O R, Grong O and Andersen S J 2001 *Acta Mater.* **49** 65-75

[30] Cheng L M, Poole W J, Embury J D and Lloyd D J 2003 *Metall. Mater. Trans. A* **34A** 2473-2481

[31] Westermann I, Hopperstad O S, Marthinsen K and Holmedal B 2009 *Mat. Sci. Eng.* **524** 151-157

[32] Westermann I, Hopperstad O S, Marthinsen K and Holmedal B 2010 *J. Mater. Sci.* **45** 5323-5331

[33] Westermann I, Hopperstad O S, Marthinsen K and Holmedal B 2012 *Int. J. Mater. Res.* **103** 603-608

[34] Barlat F and Vasudevan A K 1991 *Acta Metall. Mater.* **39** 391-400

[35] Gracio J J, Barlat F, Rauch E F, Jones P T, Neto V F and Lopes A B 2004 *Int. J. Plasticity* **20** 427-445

[36] Campbell K, Dover I, Ramachandran T R and Embury J D 1979 *Met. Forum* **2** 229-235

[37] Friis J, Holmedal B, Ryen O, Nes E, Myhr O R, Grong O, Furu T and Marthinsen K 2006 Aluminium Alloys 2006, Pts 1 and 2 519-521 1901-1906

[38] Nord-Varhaug K, Forbord B, Benestad J, Pettersen T, Ronning B, Bardal A, Benum S, Marthinsen K and Nes E 2000 *Mater. Sci. Forum* **331-3** 1387-1392

[39] Ryen Ø, Holmedal B, Li S, van Houtte P, Roven H J and Nes E 2004 in: J.F. Nie, A.J. Morton, B.C. Muddle (Eds.) *Proceedings of the 9th International Conference on Aluminium Alloys,* Institute of Materials Engineering Australasia, Brisbane, Australia, pp. 1004-1009.

[40]   Doherty R D and Mcbride J 1993 *Aluminum Alloys for Packaging* 347-368

[41] Suni J P, Shuey R T and Doherty R D 1994 in: T.H. Sanders, E.A. Starke (Eds.) *Aluminum Alloys - Their Physical and Mechanical Properties*, The Georgia Institute of Technology Atlanta, pp. 521-528

[42] Deschamps A, Esmaeili S, Poole W J and Militzer M 2000 *J. Phys. Iv.* **10** 151-156.

[43] Deschamps A, Niewczas M, Bley F, Brechet Y, Embury J D, Le Sinq L, Livet F and Simon J P 1999 *Philos. Mag. A* **79** 2485-2504

[44] Roters F, Raabe D and Gottstein G 2000 *Acta Mater.* **48** 4181-4189

[45] Donnadieu P, Dirras G F and Douin J 2002 *Aluminum Alloys 2002: Their Physical and Mechanical Properties* Pts 1-3 396-4 1019-1024

[46] Brown L M and Stobbs W M 1971 *Philos. Mag.* **23** 1185-1233

[47] Sinclair C W, Embury J D, Weatherly G C, Conlon K T and Engler O 2003 *Mater. Sci. Tech-Lond.* **19** 1321-1329

[48] Ryen O, Laukli H I, Holmedal B and Nes E 2006 *Metall. Mater. Trans. A* **37A** 2007-2013